Plastic Deformation of Semicrystalline Polyethylene under Extension, Compression, and Shear Using Molecular Dynamics Simulation

Citation: Kim, Jun Mo, Rebecca Locker, and Gregory C. Rutledge. "Plastic Deformation of Semicrystalline Polyethylene Under Extension, Compression, and Shear Using Molecular Dynamics Simulation." Macromolecules 47, no. 7 (April 8, 2014): 2515–2528.

As Published: http://dx.doi.org/10.1021/ma402297a

Publisher: American Chemical Society (ACS)

Persistent URL: http://hdl.handle.net/1721.1/96081

Version: Author's final manuscript: final author's manuscript post peer review, without publisher's formatting or copy editing

Plastic Deformation of Semicrystalline Polyethylene under Extension, Compression, and Shear using Molecular Dynamics Simulation

Jun Mo Kim[1], Rebecca Locker[2]and Gregory C. Rutledge[1]

[1]*Department of Chemical Engineering, Massachusetts Institute of Technology, 77 Massachusetts Avenue, Cambridge, Massachusetts 02139 USA*

[2]*ExxonMobil Research and Engineering Company, 1545 Route 22 East, Annandale, New Jersey 08801 USA*

[*]Corresponding author email address: rutledge@mit.edu

Abstract

Plastic deformation of the stack of alternating crystal and amorphous layers typical of semicrystalline polyethylene is studied by molecular dynamics simulation. A previous investigation of the semicrystalline layered stack undergoing isochoric extension[1] is extended here to include several new modes of deformation: iso-stress extension, iso-stress compression, and isochoric shear, at 350 K and deformation rates of 5×10^7 $s^{-1}$and 5×10^6 s^{-1}. The observed stress-strain responses are interpreted in terms of the underlying structural evolution of the material for each mode of deformation. Under tensile deformation,

crystallographic slip was observed at low strains ($0 < e_3 < 0.08$) regardless of deformation rate. Different yield mechanisms were observed for the different deformation rates. To explain the response at intermediate strains ($0.08 < e_3 < 0.26$), we introduce the concept of "bridging entanglements", which are temporary, physical bridges between crystal lamellae comprising entanglements involving chain segments belonging to different crystal lamellae. At high strains ($e_3 > 0.26$), melting and recrystallization was observed at the slower deformation rate, while surface melting and cavitation were observed at the faster deformation rate. Under compressive deformation at the slower deformation rate, crystallographic slip was again observed at low strains. For the faster compressive deformation, an initial period of rapid stress growth at low strain was observed. This initial stress growth then transitions to a process of fine crystallographic slip at a strain of $e_3 = -0.005$. At intermediate strains under compressive deformation, the release of bridging entanglements is observed for both strain rates. However, no melting or recrystallization phenomena were observed under compression, even at the highest strains simulated ($e_3 = -0.33$). Under shear deformation, interlamellar slip was observed for both zx and zy shear (strain gradient parallel to stacking direction). Chain segments tend to stretch and align in the shear direction. Interestingly, under shear deformation this semicrystalline polyethylene exhibits transient behavior typical of non-Newtonian fluids.

Introduction

When polymers are crystallized in the bulk, they generally do not crystallize completely[2], and the resulting final morphology is generally believed to be determined by the kinetics of crystallization. This "semicrystalline" state is stable over the useful lifetime of the polymer. Semicrystalline polymers therefore consist of at least two components: the ordered crystalline domains and the disordered noncrystalline domains. The noncrystalline domains are often further subdivided into an amorphous part and an "interphase" of finite width that exists at the crystal/amorphous domain boundary[3-5]. Since the crystalline and noncrystalline domains are typically on the order of 1-10 nm in thickness, much less than the coil dimension of the typical high molecular weight polymer, molecular chains traverse from one domain to another, often multiple times, resulting in the formation of several segment populations; helical conformers in the crystal domains are often called "stems", while bridges (or tie chains), loops and tails make up the noncrystalline domains[6,7]. Due to these unique structural and morphological characteristics, semicrystalline polymers are remarkably tough and stiff, and have found widespread use in contemporary life.

The simplest motif in the semicrystalline polymer morphology is the lamellar stack, consisting of alternating layers of crystalline lamellae and noncrystalline domains, whose signature is the strong peak in small angle X-ray scattering identified with the long period, or repeat length, of the stack. This long period is on the order of 20 nm, in contrast with the lateral dimension of the lamellae, which is on the order of micrometers. More complex morphological variations depend on how these lamellar stacks are organized in three-dimensional space. Depending on the conditions under which the material is crystallized, the lamellar stacks may be arranged into hedrites, spherulites or related morphologies, with a distribution in orientation of the lamellar stacks with respect to the sample axes. The lamellar stacks may be subject to gradual deviations and twist in stack orientation, or sharp

discontinuities at grain boundaries.

Altering the structural, topological or morphological characteristics of the semicrystalline material changes the mechanical behavior of semicrystalline polymers significantly. For example, the yield stresses of semicrystalline polymers are known to vary with the thickness of the crystalline lamellae[8]. Numerous experiments on semicrystalline polymers have been performed since the 1960s in order to clarify the relation between structure and mechanical properties of the semicrystalline state of matter; excellent reviews are available[9,10]. Nevertheless, detailed analysis of the connection between molecular structure and topology and morphology, on the one hand, and mechanical response on the other has defied molecular level description. This is due, in part, to the hierarchical organization of crystal and amorphous domains into a complex, e.g. spherulitic, morphology and by an inability to distinguish and measure the number, length and organization of segments in the various populations of the noncrystalline domains. For example, there have historically been two opposing models for the distribution of loops on a lamellar crystallite in the semicrystalline material. In the "adjacent re-entry" model[6], loops connect stems in neighboring crystallographic sites, in the form of regular, short folds, while in the "switchboard" model[11], loops connect stems randomly throughout the crystal lamellae in an irregular fashion. Only with molecular models that account simultaneously for crystal symmetry, chain connectivity and excluded volume has it been possible to resolve this long-standing debate[12,13].

Plastic deformation of semicrystalline polymers (i.e. solid state processing) can also be used to improve the mechanical properties of semicrystalline polymers significantly. However, because of the complex structure of semicrystalline polymers, understanding of plastic deformation processes in semicrystalline polymers is not an easy task; it demands a hierarchical, multi-level approach in which processes that occur on disparate time and length

scales are treated at different levels of description: microscopic, mesoscopic, or macroscopic[14, 15]. Experiments alone have not been able to elucidate this complex structure and multi-level response of semicrystalline polymers. For example, WAXS is often used with deformation to follow microscale mechanisms in crystal domains. However, it cannot characterize deformation of the noncrystalline domain fully. Thus, there is a need for approaches that shed light on some of these other aspects of deformation in semicrystalline polymers. Hierarchical, multi-scale simulations of semicrystalline polymers can be good tools for this purpose and for interpreting the mechanisms behind the experimental results.

We have previously reported the use of lattice dynamic and Monte Carlo simulations to estimate the full elastic stiffness and compliance tensors for both the crystalline[16,17] and noncrystalline domains[13], in the limit of small strain. More recently, we have begun to explore the elastic-plastic response of the lamellar stack at large strain. The first such study involved simulations of plastic deformation in semicrystalline polyethylene under conditions of tensile deformation with either constant lateral dimensions or at constant volume[1]. In a complex morphology, however, many modes are likely to be present simultaneously at different spatial locations. In this work, we extend our previous study to include other important deformation modes, such as compression and shear, required to describe fully the response of a complex arrangement of lamellar stacks under an arbitrary load. Each mode of deformation is defined by the conditions of shear and strain (or strain rate) applied in each direction to a representative volume element of the material. Ultimately, we envision that the properties extracted by simulation at the molecular level can be used to inform a finite element simulation or similar[18-20], in a multi-scale approach to modeling the complex but vitally important mechanical behavior of semicrystalline polymers.

Models and Simulation Methodology

1. Interphase Model by Monte Carlo

The ensembles of configurations of semicrystalline polyethylene used in this work were generated using the Interphase Monte Carlo (IMC) method, which has been developed in a series of papers[12, 13, 21-24]. Briefly, the models generated by the IMC methodology consist of a noncrystalline domain sandwiched between two static crystalline domain boundaries. Both crystalline and noncrystalline domains are rendered semi-infinite in the lateral dimensions through the use of periodic boundary conditions. The density of the noncrystalline domain is chosen so that it does not crystallize, whereas the static crystalline boundaries preclude formation of a completely amorphous noncrystalline domain. The result is a model of the semicrystalline lamellar stack that is rigorously metastable. The thickness of the interphases and the variation of order parameters through their thickness are not constrained, but are dictated instead by the equilibration of the model subject to the constraints described above. In order to sample both the spatial packing of atomic sites and the topological phase space of bridges, loops and tails that are consistent with the imposed density and boundary conditions, Monte Carlo moves are employed that displace sites and that alter chain connectivity to create new loops, bridges and tails. Tails are the result of a small number of chain end atoms that are introduced to improve the efficiency of the connectivity-altering moves and to set the number average molecular weight of the polymer. The model is illustrated in Figure 1. The interested reader is referred to previous reports for the details of the method. The resulting model is simulated in the ($NN_{end}VT$) ensemble, corresponding to a fixed number of sites, fixed number of end sites, constant volume and constant temperature.

A united-atom (UA) force field, originally developed by Paul *et al.*[25] and modified as described by Bolton *et al.*[26] and In't Veld *et al.*[24], was used in this work. This force field was originally developed to describe the structure and dynamics of polyethylene melts, where

the results were compared to those obtained using an all-atom force field. The glass transition temperature of C1000 using this force field has been estimated to be 223 K, based on the change in thermal expansion coefficient with temperature, extrapolated to zero cooling rate[27]; this value is in good agreement with the value of 237 K for polyethylene, based on experimental data.[28] In our own experience, this force field also reproduces well the melting points of n-alkanes and the heats of fusion for the rotator phases of n-alkanes[29]. Being a united atom force field, it does not generally capture the orthorhombic or lower symmetry of many n-alkane and polyethylene crystal lattices. The rotator phase may permit greater mobility within the crystal domain during deformation, but is believed to have little influence on the topological nature of the crystal/amorphous interphase. For further details, the reader is referred to the original works.

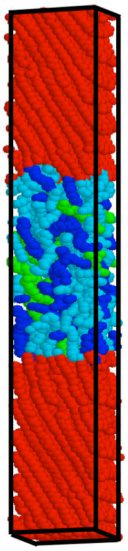

Figure 1. Semicrystalline polyethylene model for this work. Red sites denote stems in the crystalline domains, while cyan, green and blue sites denote loops, bridges and tails, respectively, in the noncrystalline domain. Periodic boundary conditions are applied in all directions.

Using the Interphase Monte Carlo method, an ensemble of configurations of semicrystalline polyethylene was generated. Each system was first populated with a crystal lattice of 3 × 5 × 100 unit cells (a × b × c). As shown in Figure 1, the chain stems in the crystal phase were tilted so that the {201} crystallographic plane is normal to the lamellar stack, or z-direction, corresponding to the most probable crystal-amorphous interphase, as determined experimentally by Bassett *et al.*[30] and computationally by Gautam *et al.*[21]. In order to satisfy periodic boundary conditions with an orthorhombic lattice that is rotated about its b-crystallographic axis (corresponding to the y-axis of the simulation cell), the simulation cell was necessarily monoclinic. Seventy-four sites were then removed from each of six randomly selected chains in the system to create a noncrystalline domain density of 0.8 g/cm^3, comprising 24 bridge or loop segments and 12 tail segments. The unit cell lattice parameters were then adjusted to ensure stresses in the crystal phase corresponding approximately to atmospheric pressure at T = 350 K, following the prescription of Hütter *et al.*[12]. The dimensions of the final simulation box were L_x=2.742, L_y=2.368, and L_z=21.613 nm, with angles of $\alpha = \gamma = 90°$ and $\beta = 89.98°$. A 10.8 nm thick section near the midplane of the simulation cell and comprising 2556 UA was then subjected to amorphization using Interphase Monte Carlo simulation, while the remaining sites were held fixed in their crystallographic positions. After an initial randomization of structure and topology at 10000 K for 10000 Monte Carlo cycles, the system was cooled stepwise in 0.4825 K/MC cycle increments to 350 K, and ten samples were drawn at equal intervals from a simulation of 40000 cycles at 350 K, in the same manner as reported by Lee and Rutledge[1]. For further details of the model generation method using IMC, the reader is referred to that work.

2. Semicrystalline Model

To model the full semicrystalline lamellar stack, the ensemble of ten configurations

generated by the IMC methodology were imported to LAMMPS[31] and equilibrated by molecular dynamics (MD) in the ($NN_{end}PT$) ensemble for 8 ns, as described previously[1]. Molecular dynamics simulation effectively thermalizes both the crystalline and noncrystalline domains, but does not alter the topology of the configuration significantly. To rectify a discrepancy found in the work of Lee and Rutledge[1], all configurations were equilibrated in LAMMPS with the long range corrections to pressure and energy included, using a time step of 2 fs for all interactions. Temperature and pressure were maintained at 350K and 0.1 MPa using a Nóse-Hoover thermostat and barostat (temperature damping parameter was 10 time steps and stress damping parameter was 1000 time steps)[32]. Each diagonal component of the pressure tensor was controlled independently. Although crystallization of the inter-lamellar domain was in principle possible during molecular dynamics simulation of the Semicrystalline Model (because density of the noncrystalline domain was no longer constrained), the system remained in its metastable state with constant crystallinity for the duration of equilibration. After equilibration in LAMMPS, the dimensions of the simulation box were L_x=2.742 ± 0.086, L_y=2.368 ± 0.013, and L_z=21.613 ± 0.670 nm, with angles of $\alpha = \gamma = 90°$ and $\beta = 89.98°$. More details of the fully thermalized semicrystalline model generation using IMC and molecular dynamics can be found in Lee and Rutledge[1].

3. Topological analysis

The topology of the semicrystalline state is characterized by the number and length of each of the four populations of chain segments: crystal stems, and noncrystalline bridges, loops and tails. Here we present a general algorithm to classify every segment in the simulation into one of these four populations. First, all end sites are located and the sequences of sites that comprise each chain running from one end site to another are identified (“chains”). As currently implemented, IMC permits the formation of cycles

containing two or more crystal stems; the algorithm described here can be augmented to identify such cycles after all linear chains are counted. There were no cycles among the ten configurations used in this study. Next, a local order parameter is used to label the site as either crystalline or noncrystalline; for this purpose, we use the local orientational order parameter $P_{2,i} = \left(3\left\langle \cos^2 \theta_{ij} \right\rangle - 1\right)/2$ computed for each site *i*. Here, θ_{ij} is the angle between the vector from site *i-1* to *i+1*, and that from *j-1* to *j+1*; the average is taken over all sites *j* within a cutoff distance $r_c=2.5\sigma$ of site *i*, where σ is the UA van der Waals diameter. All sites having $P_{2,i}> 0.4$ are designated as crystalline. To filter out spurious "short" segments that arise due to thermal variations in $P_{2,i}$, sequences of atoms of one type (crystalline or noncrystalline) less than 4 beads long are "flipped" to the other type. After this filtering, any sequence of crystalline sites is designated a "stem". A sequence consisting of an end site and any consecutive noncrystalline sites is designated a "tail". All other sequences of noncrystalline sites are necessarily loops or bridges. Bridges are identified as those remaining sequences for which the change in z coordinate from the first to last site of the sequence is larger than $L_z/2$ times the fraction of noncrystalline sites. Finally, all remaining sequences are identified as loops. As a result of this algorithm, the numbers and lengths of stems, bridges, loops, and tails for the 10 configurations were determined, as reported in Table 1. Among the 10 configurations, 5 configurations have one bridge segment, and the rest have none. On average, the configurations in this data set consist of 3.1% bridge sites, 10.27% loop sites, and 32.97% tail sites (defined as the total number of sites in each population divided by the total number of sites in the configuration, averaged over all 10 configurations); the balance consists of stem sites. From these numbers, one can compute an average crystallinity of 53.7% and an average crystal stem length of 99.4 sites after equilibration by molecular dynamics.

4. Simulated Deformation Methodology

Nonequilibrium molecular dynamics (NEMD) simulations were performed for the following modes of deformation of semicrystalline polyethylene: uniaxial extension in the lamellar stack direction (z-direction) with constant lateral stresses, compression in the lamellar stack direction with constant lateral stresses, and transverse shear deformation in the two directions lateral to the stack direction. The NEMD simulations were performed using open source code for the LAMMPS package[31]. The equations of motion with Nose-Hoover thermostat and barostat were integrated using the Verlet algorithm[33] with time step of 2 fs. The instantaneous temperature was computed in the usual way from kinetic energy and regulated to a mean value of 350 K; using the "remap x" command in LAMMPS, contributions to velocity due to deformation were not included; in any event, the strain contribution to molecular velocities is estimated to be less than one part in 10^5.

Table 1. Results of topological analysis for the ten configurations of semicrystalline polyethylene studied in this work.

Configuration	Stems		Bridges		Loops		Tails	
	# of stems	# of UA in stems	# of bridges	# of UA in bridges	# of loops	# of UA in loops	# of tails	# of UA in tails
1	30	2998	1	228	23	811	12	1519
2	30	2965	1	138	23	434	12	2019
3	30	2994	1	482	23	309	12	1771
4	30	2971	1	575	23	383	12	1627
5	30	2957	1	298	23	637	12	1664
6	30	2990	0	0	24	280	12	2286

7	30	2968	0	0	24	1030	12	1558
8	30	2987	0	0	24	852	12	1717
9	30	2992	0	0	24	374	12	2190
10	30	2996	0	0	24	595	12	1965

The total instantaneous stress tensor was computed according to the method of Irving and Kirkwood[34]. Uniaxial extension was performed at a constant positive strain rate $\dot{\varepsilon}_3$ (Voigt notation) where the subscript '3' refers to the direction parallel to the direction of stack alternation (z-direction), and lateral dimensions were held at constant (0.1MPa) stress (the $NN_{end}\sigma_x\sigma_y\varepsilon_z T$ ensemble). The observed modulus for this mode of deformation corresponds to the elastic compliance, S_{33}. This contrasts with the previous study of Lee and Rutledge[1], where extensional deformations were performed at constant lateral dimension (corresponding to the elastic stiffness, C_{33}) or constant volume. In conjunction with the results of Lee and Rutledge for tensile deformation, this part of the study provides upper and lower bounds on the elastic and plastic responses for semicrystalline polyethylene in extension. Similarly, uniaxial compression refers to negative strains ε_3, with lateral dimensions held at constant (0.1 MPa) stress. Finally, results are reported for transverse, or inter-lamellar, shear, in which the z-plane of the simulation was displaced in the x- or y-direction (ε_4 or ε_5, respectively, in Voigt notation). Experimentally, inter-lamellar shear modes have been shown to be relatively soft above T_g, compared to other modes of amorphous phase deformation such as inter-lamellar separation and stack rotation[9, 35, 36]. Recent work by Brown and coworkers indicates that, within certain limitations, the full stress-strain response for high density polyethylene (HDPE) in compression obeys a linear time-temperature superposition with a one-decade increase in strain rate being approximately equivalent to a 10

K drop in temperature[37,38]. Even allowing for deformation rates in simulations that are seven to eight orders of magnitude higher than conventional experiment deformation rates, the deformations simulated here should be well above the glass transition.

For each mode of deformation, true strain rates ($\dot{\varepsilon}$) of 5×10^7 $s^{-1}$and 5×10^6 s^{-1} were employed, and are henceforth designated "fast" and "slow", respectively. By comparison, the best available estimate of Rouse time for a simulated melt of C150 at 350 K using the current force field is about 10^{-7} s,[27] for which the corresponding Weissenberg numbers (Wi) would be 5 and 0.5 for fast and slow deformations, respectively. The number average length of segments in the noncrystalline domain is about 70-75, but these segments are also constrained in part by their coupling to the dynamics of the crystalline domain, so that these values of Wi are only approximate.

The interfaces between the crystalline and amorphous domains were identified with the Gibbs dividing surface[12], defined by

$$\rho_{int} = \int_{-\infty}^{\infty} (\rho(z) - \rho^{step}(z \mid z_{div}))\, dz = 0. \qquad (1)$$

where $\rho(z)$ is the areal density of UA as a function of z position, and $\rho^{step}(z|z_{div})$ is a step function in density from the crystalline domain value to the amorphous value at z_{div}; the location of the Gibbs dividing surface, z_{div}, is chosen so that Eq 1 is satisfied.

5. Analysis of Entanglement Statistics

In order to analyze entanglement properties of semicrystalline polyethylene such as the primitive path of each segment, the number of entanglements, the number of UA between entanglements (N_e), and so on, we employed the Z code developed by Kröger[39]. The primitive path (PP) is defined as the shortest path connecting the two ends of a chain with the same topology as the chain itself. "Kinks" occur where two chains cross one another and

result in a point of contact that limits further reduction of the primitive path. Such kinks are topological constraints and have been identified with physical entanglements. In addition, we developed an algorithm to identify a subgroup of entanglements henceforth denoted "bridging entanglements" (*c.f.* Figure 2). In this algorithm, we applied the Z code to only the amorphous domain to obtain PP's of the amorphous segments. Then we classified these PP's into bridges, loops, and tails using the aforementioned topological analysis algorithm. Next, for each "kink" of a loop or tail PP connected to one crystalline domain, the distance was calculated to all kinks of loop and tail PP's connected to the other crystalline domain. If any of these distances is found to be less than σ, the van der Waals distance used in the nonbonded interaction potential, we classify the pair of segments as a bridging entanglement. Bridging entanglements are believed to act as temporary, physical bridges, in much the same way that entanglements in melts act as temporary, physical crosslinks in an entanglement network. Note that other approaches have been proposed to identify tie chains and "trapped entanglements"[40].

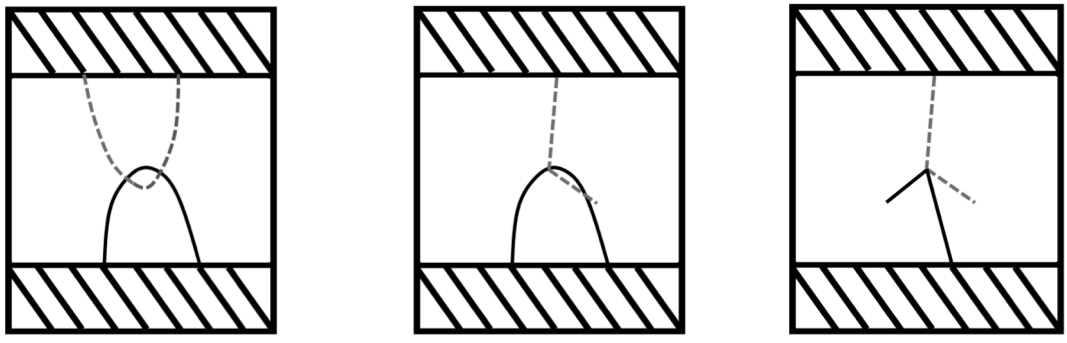

(a) (b) (c)

Figure 2. Examples of bridging entanglements. (a) loop-loop bridging entanglement; (b) loop-tail bridging entanglement; (c) tail-tail bridging entanglement

Results and discussion

1. Uniaxial Extension and Compression

Previously, Lee and Rutledge reported results for uniaxial extension in the direction of the lamellar stack (z-direction) for the case of fixed lateral dimensions and for the case where lateral dimensions were changed equally to maintain constant volume; compression was not investigated in that work. Depending on the mode of extensional deformation and the deformation rate, several responses were observed, ranging from fine crystallographic slip at low strain, in accord with experimental observations[15], to cavitation or melting at high strain, for fast and slow deformations, respectively. Cavitation is typical of dilatational deformations like uniaxial extension with constant lateral dimensions. However, other modes of deformations such as compression and shear are not dilatational by nature, and should therefore yield by some other mechanism; the mechanisms responsible for plasticity at large strain must thus be evaluated mode by mode, and as functions of strain rate. In this section, we extend the previous results for uniaxial extension of the lamellar stack to the case of constant lateral stress, and consider compression as well as extension. In both uniaxial extension and compression, deformation was imposed in the direction of the lamellar stack (the z-direction) with two different deformation rates (fast and slow deformations) under constant lateral stresses ($\sigma_1=\sigma_2$ = 0.1 MPa) at 350 K.

Figure 3 shows the zz component of the stress tensor (σ_3 in Voigt notation) as a function of engineering strain (e_3) for both fast and slow deformations under uniaxial extension and compression. The response under extensional deformation may be broken down into 3 parts, based on magnitude of strain. At low extensional strains ($0 < e_3 < 0.08$), the stress-strain behavior under slow deformation (Fig 3a) is linear and reversible (as confirmed by simulations in which the extensional deformation was run in reverse), with an elastic modulus (corresponding to the inverse of the compliance, $E_3=1/S_{33}$) of 0.08±0.009GPa in the range -

$0.02 < e_3 < 0.02$. By contrast, the stress-strain behavior under fast deformation (Fig 3b) exhibits an elastic modulus of 0.143±0.015GPa for strains in the range $-0.02 < e_3 < 0.02$. The strain rate-dependence of the apparent elastic modulus may be attributed to differences in the activation of molecular relaxation processes during both elongation and recovery, for strain rates that are comparable to molecular relaxation rates. The elastic stiffness C_{33}, obtained for uniaxial extension with constant lateral dimensions reported by Lee and Rutledge[1] was 0.72±0.04 and 0.83±0.05 GPa for slow and fast deformations, respectively. In general, elastic stiffnesses are larger than elastic moduli, as is confirmed to be the case here.

As shown in Figure 4, the x and y dimensions of the lamellar stack contract at different rates under constant lateral stress, due to the anisotropic nature of crystalline lamellae. In the $N\sigma_x\sigma_y l_z T$ ensemble, the x dimension of semicrystalline polyethylene shrinks more rapidly than the y dimension for both fast and slow tensile deformations. The corresponding Poisson's ratios are ν_{13} =0.96±0.02 and ν_{23} = 0 for both fast or slow deformation, up to e_3=0.10. This is in contrast to the transversely isotropic dimensional changes assumed by Lee and Rutledge[1] for the isochoric extensional deformation. Lee and Rutledge[1] reported elastic constants of 0.175±0.003GPa and 0.160±0.005GPa for fast and slow deformations, respectively under constant volume conditions. As expected, the elastic constants obtained for isochoric uniaxial extension under fast and slow deformation rates are intermediate between the elastic stiffnesses (upper, Voigt bound) and elastic moduli (lower, Reuss bound). It is also possible to compare the elastic responses obtained here to those reported by Veld *et al.*[13] for the interlamellar domain alone, using the IMC model. They reported $1/S_{33}$=0.27 GPa by taking the inverse of the full elastic stiffness tensor with monoclinic symmetry, obtained by Monte Carlo simulations. That value is significantly higher than the values obtained here, suggesting that uniaxial extension of the lamellar stack involves the crystalline lamellae as well as the interlamellar domain, even at low strain.

At intermediate extensional strain ($0.08 < e_3 < 0.26$), the lamellar stack exhibits strain hardening, with the stress increasing dramatically for both strain rates and leveling off around e_3=0.26 for both fast and slow deformations. From the snapshots of fast deformation under extension in Figure 5(b), cavitation is observed at high strains, beyond $e_3 \sim 0.26$. At still higher extensions, a variety of responses were observed, ranging from dramatic strain hardening to a dramatic strain softening, which we believe may be due to fracture of the system in the presence or absence, respectively, of bridges or bridging entanglements. Since fracture is probably sensitive to the finite size of the simulations, we have excluded from Figure 3(b), and subsequent analysis of fast extensional deformation, the results of four configurations where fracture was suspected. From the snapshots of slow deformation under extension in Figure 5(a), no such cavitation or fracture is evident; an alternative mechanism of yield due to surface melting is explained below.

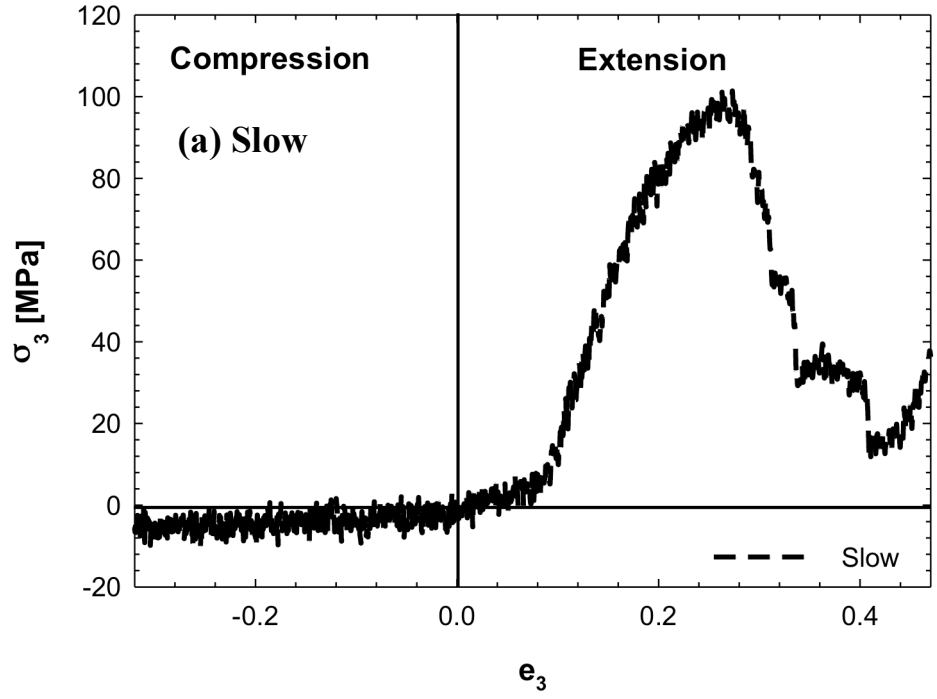

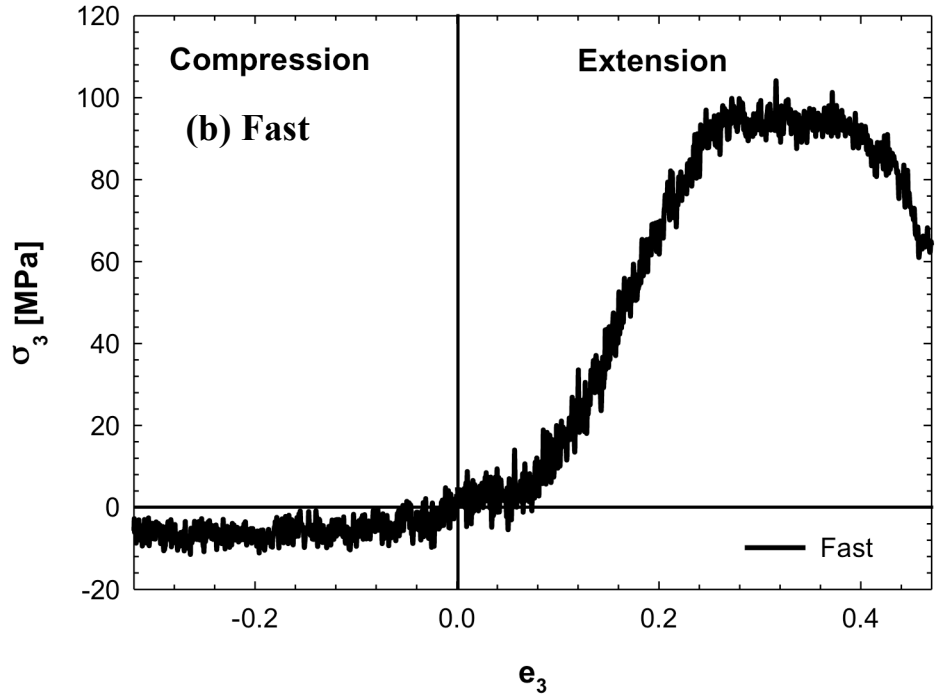

Figure 3. Stress (σ_3)-strain (e_3) curves under tensile for (a) slow and (b) fast deformations. Each curve is an average over the 10 configurations in the ensemble.

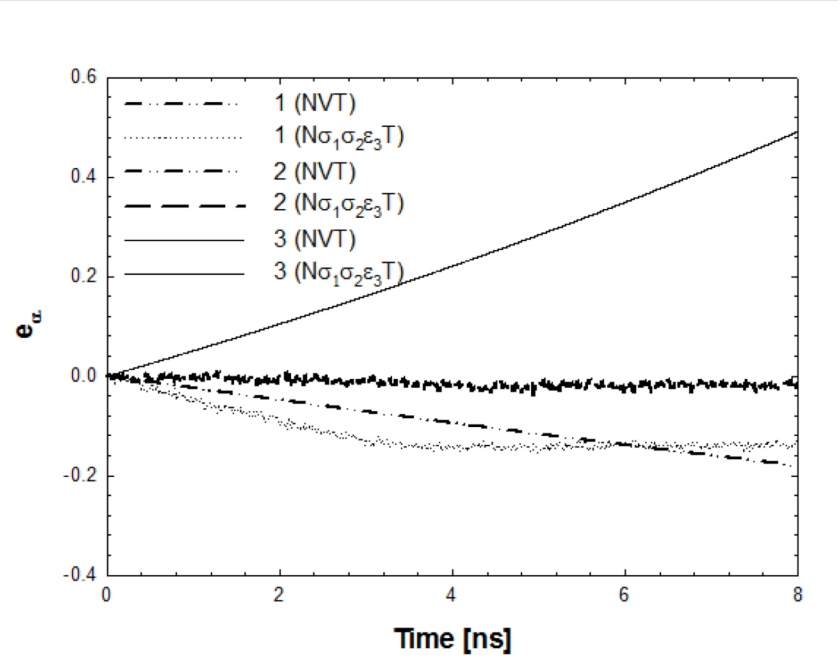

Figure 4. Engineering strains (e_α) vs. time at fast deformation under extension. The curves for e_1 and e_2 for NVT overlap at all times, by construction[1]. The curves for e_3 for NVT and $N\sigma_1\sigma_2\varepsilon_3T$ also overlap, by construction.

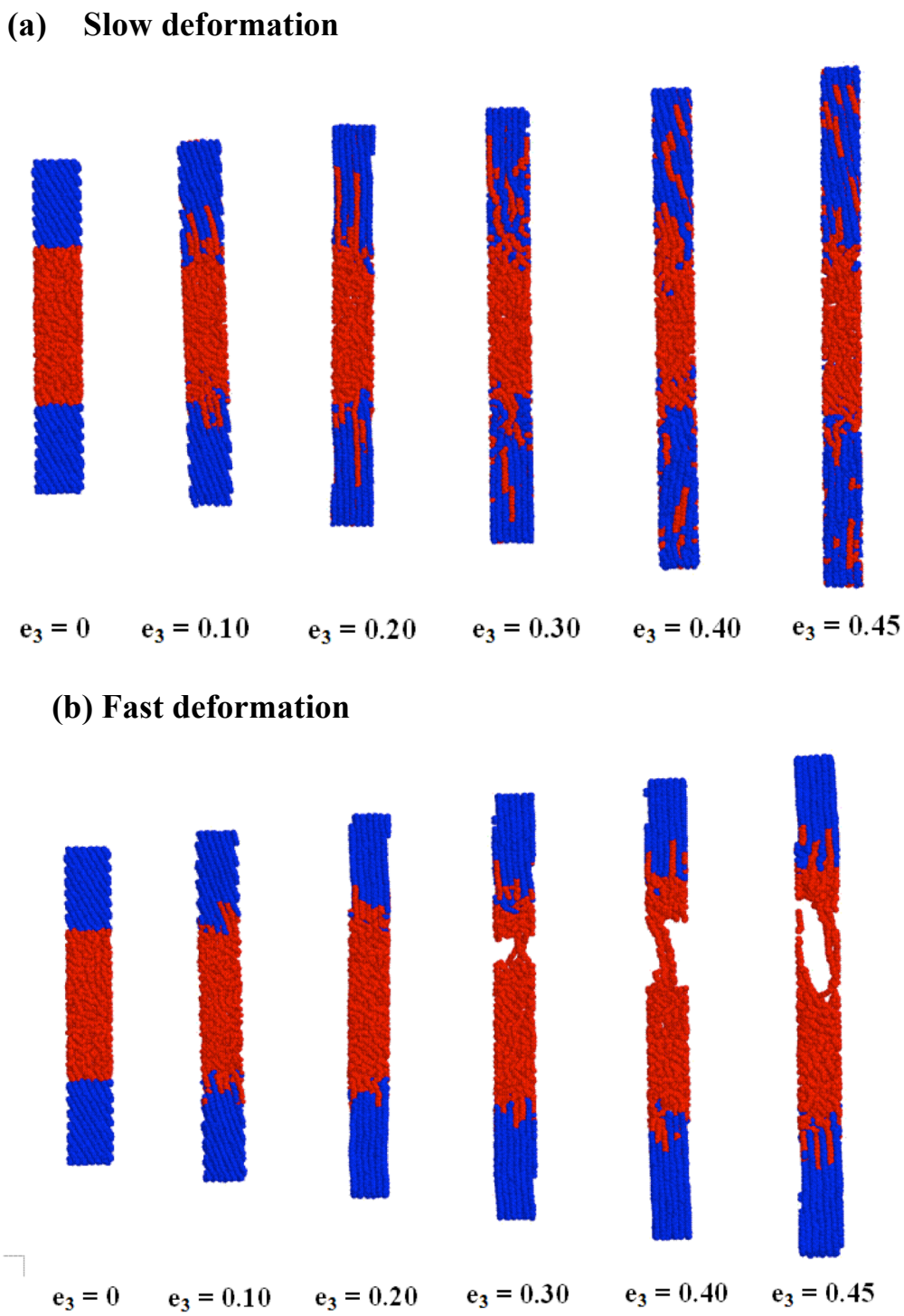

Figure 5. Snapshots from a typical configuration for (a) slow and (b) fast deformation under extension. Sites originating in the crystal domain at t=0 are shown in blue, and those originating in the noncrystalline domain are shown in red.

(a) Slow deformation

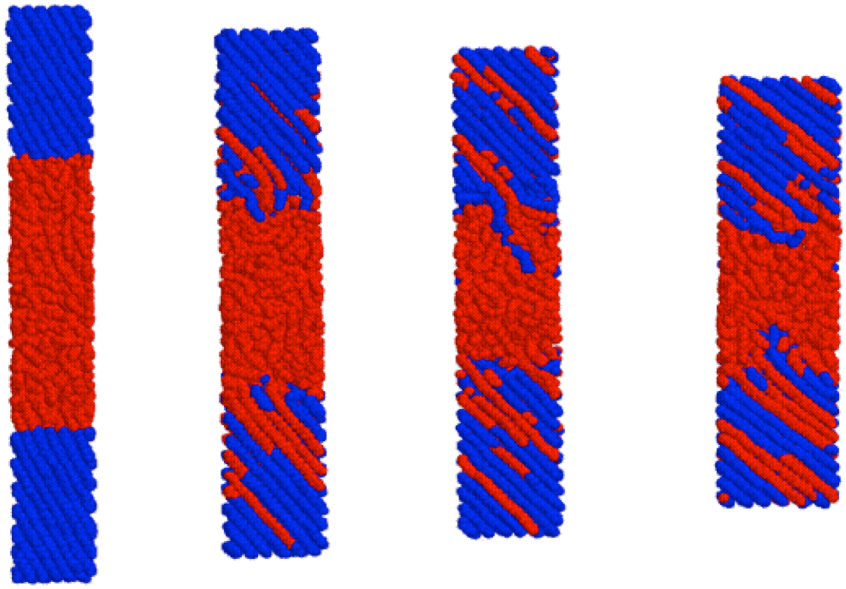

$e_3 = 0$ $e_3 = -0.1$ $e_3 = -0.20$ $e_3 = -0.3$

(b) Fast deformation

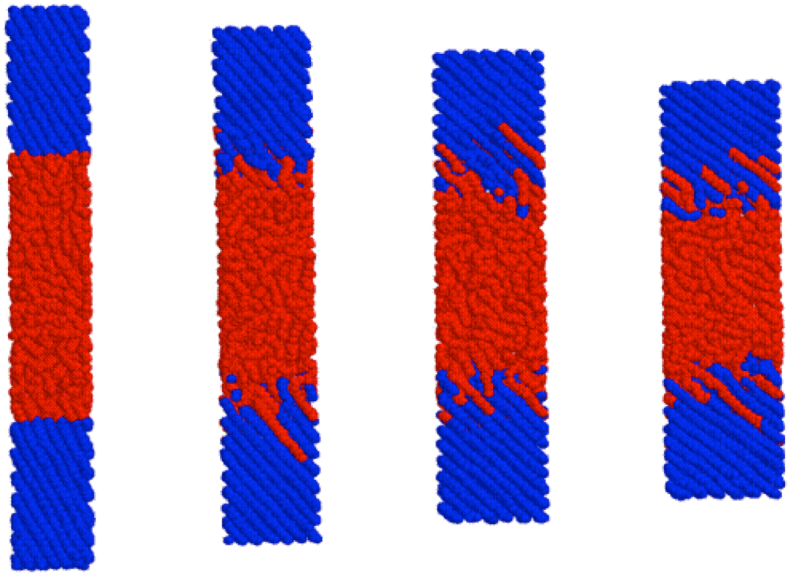

$e_3 = 0$ $e_3 = -0.1$ $e_3 = -0.20$ $e_3 = -0.3$

Figure 6. Snapshots from a typical configuration for (a) slow and (b) fast deformation under compression. Sites originating in the crystal domain at t=0 are shown in blue, and those originating in the noncrystalline domain are shown in red.

There is a drop in stress near e_3 = 0.40 for fast deformation. In the case of slow deformation, the stress-strain curve decreases dramatically through a series of steps beyond e_3 = 0.26. Reversing the strain direction from e_3=0.26 confirms that the deformation is no longer reversible and elastic at this point. We define a yield point as the strain at which this intermediate stiff response begins to soften, from the intersection of linear fits to the stress-strain data above and below the yield point. In this manner, using linear fits to the data from e_3 = 0.18 to 0.26 and from and e_3 = 0.26 to 0.40 for the fast deformation (Fig 3b), we obtain a yield stress ($\sigma_{y,fast}$) of 95±2.7 MPa at a strain of e_3 = 0.26. Using the same method for slow deformation, the yield stress ($\sigma_{y,slow}$) is found to be 77±3.0 MPa at a strain of e_3 = 0.18. These values for yield stress are higher than those reported previously under isochoric extension ($\sigma_{y,fast}$ = 40 MPa at e_3 = 0.17 and $\sigma_{y,slow}$ = 12 MPa at e_3 = 0.07)[1].

Also shown in Figure 3 are the stress vs. strain responses in compression for both fast and slow strain rates. Under fast deformation, the stress grows faster at low compressive strains ($-0.02 < e_3 < 0$) than it does under slow deformation. In this region of compressive strain, as mentioned before, the elastic constant is found to be 0.143±0.015 GPa over the strain range of $-0.02 < e_3 < -0.02$ for the fast deformation, compared to 0.08 ± 0.009 GPa over the same range of strains for the slow deformation. Beyond compressive strains of e_3=-0.02, the compressive modulus is found to be 0.0102±0.0001 GPa for the fast deformation, and 0.0113±0.0007 GPa for the slow deformation.

In order to explain the origin of the stress-strain response, the angular distribution of chain segment vectors with respect to the crystal-amorphous interface normal for the entire simulation box is shown in Figure 7, for both fast and slow deformations, under extension and compression. The peak at about 30° at zero strain is due to the [201] orientation of stems in the crystalline phase; chain segment vectors in the noncrystalline domain are more or less randomly distributed over the entire range of angles. The chain segment vectors in the

amorphous phase are randomly distributed throughout a broad range, with an average angle of 56° with respect to the crystal-amorphous interface normal, indicative of a random distribution of angle between the normal and the plane of the interface. Under uniaxial extension, it is known that segments of semicrystalline polymer in both crystalline and noncrystalline domains tend to orient towards the applied stress direction[9, 15]. From this figure and snapshots in Figure 5 and 6, the reorientation of chain segments toward the applied stress direction can be easily confirmed. In both fast and slow extensional deformation cases, the peak in the angular distribution associated with stem segments in the crystal decreases from 30° to 0° as strain increases. This shift in the peak is indicative of reorientation of stems primarily from the {201}-oriented interface to the {001}-oriented interface, beyond which further alignment is not possible. This observation is consistent with (100)[001] fine crystallographic slip during fast and slow deformations. It also explains why ν_{13} is close to unity while ν_{23} is essentially zero at low strain. This result accords well with the previous study of Lee and Rutledge[1]. For crystal lamellae of the thickness simulated here (~11 nm), such crystallographic slip is usually attributed to a defect-mediated α_c-relaxation associated with the crystal phase [41, 42].

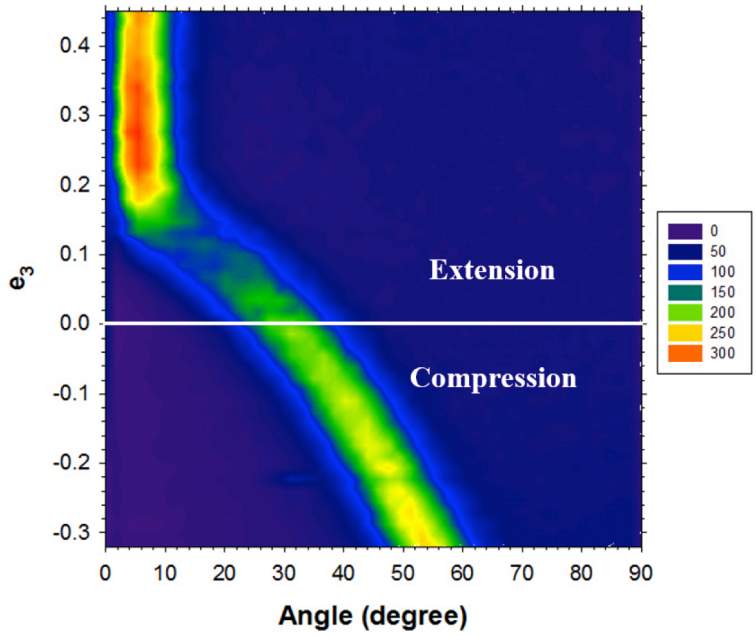

(a)

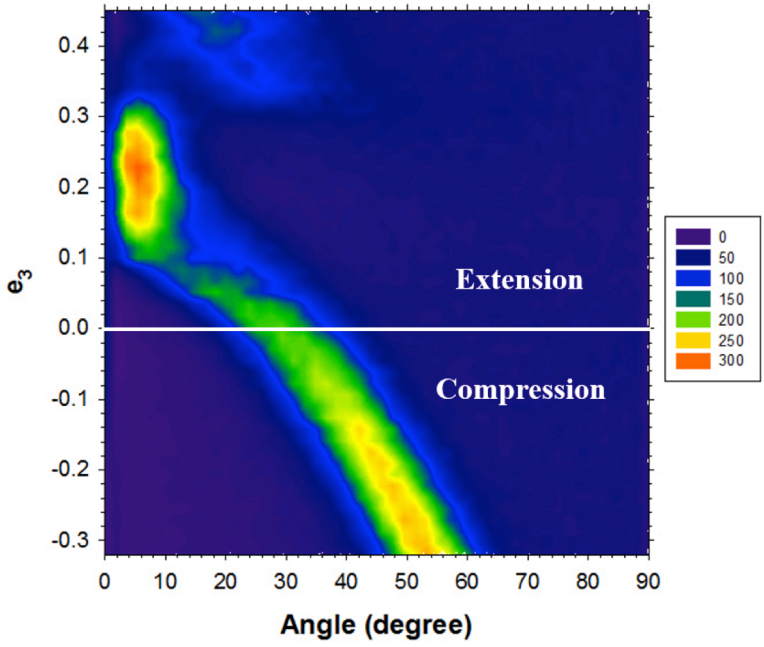

(b)

Figure 7. Angular distribution of the chain segment vectors. The orientation angle is calculated with respect to crystalline-amorphous interface normal. (a) Fast deformation; (b) Slow deformation under uniaxial extension and compression;

At intermediate extensional strains ($0.08 < e_3 < 0.26$) for both fast and slow deformations, the chain segment vectors complete their rotation toward the direction of applied stress and align to the {001} interface. At high strains ($e_3 > 0.26$), the angular distribution of the chain segment vectors for slow deformation become dispersed over a wide range of values, which is associated with the step-wise drops in stress in the ensemble-averaged stress-strain curve of Figure 3(a). This behavior is due to twinning in the crystal domain under slow deformation. Note that twinning under slow extensional deformation can be verified in Figure 5(a) at $e_3 = 0.30$. No such twinning is observed under fast deformation.

Figure 7 also shows the angular distribution of chain segment vectors as a function of compressive strain for both fast and slow deformations; their response in compression is qualitatively the same. During uniaxial compression, the chain segment vectors in the crystalline phase rotate away from the direction of applied stress, as evidenced by the shift in the peak (primarily due to crystal stems) in Figure 7 from 30° to 54°. The shift of chain segment vectors away from the direction of compression can also be seen in the snapshots of Figure 6. Because fine crystallographic slip is the only operative mechanism here, there is no distinct yield event up to $e_3 = -0.32$. There are no other mechanisms, such as stretching of chains, cavitation, or melting and recrystallization, operative in compression.

Under tensile deformation, the entangled amorphous network is believed to play an important role in semicrystalline polymers[43]. In order to investigate this effect, we calculated various entanglement statistics using the Z code. In Table 2, we report the average length in Ångstroms between entanglements of PP segments ($<d_e>$) and the average number of atoms between entanglements ($<N_e>$) as functions of strain. These values are in reasonable accord with previously reported values for polyethylene (C400) melts at comparable strain rates ($<d_e>\sim19$, $<N_e>\sim30$).[44] These values fluctuate within ~5% of their averages from $e_3=0$ up to $e_3=0.26$. By $e_3=0.34$, $<d_e>$ has increased faster than $<N_e>$,

indicative of stretching of PP segments. To investigate stretching of PP segments between entanglements, we show in Figure 8(a) the distributions of lengths of primitive path (PP) segments as functions of applied strain. The general trend with increasing strain is towards the elimination of PP segments of intermediate length. This is shown more clearly in Figure 8(b), where PP segment distributions at zero strain and at an extensional strain of 0.34 have been singled out for comparison. Notably, the population of long PP segments (> 50Å) is larger at e_3=0.34. By e_3=0.45, however, both $<d_e>$ and $<N_e>$ have dropped significantly; we attribute this drop to the onset of melting (*c.f.* Fig 13 below), which provides a mechanism by which the noncrystalline domain can relax.

Table 2. Average length of primitive path (PP) segments between entanglements ($<d_e>$) at different strains and the average number of atoms between entanglements ($<N_e>$) under fast deformation. Both properties are averaged over all 10 configurations.

Strain	$<d_e>$ (Å)	$<N_e>$	$<d_e>/<N_e>$
0	17.08	35.22	0.48
0.08	16.97	38.49	0.44
0.26	17.97	37.71	0.47
0.34	19.17	38.43	0.50
0.45	18.04	32.12	0.56

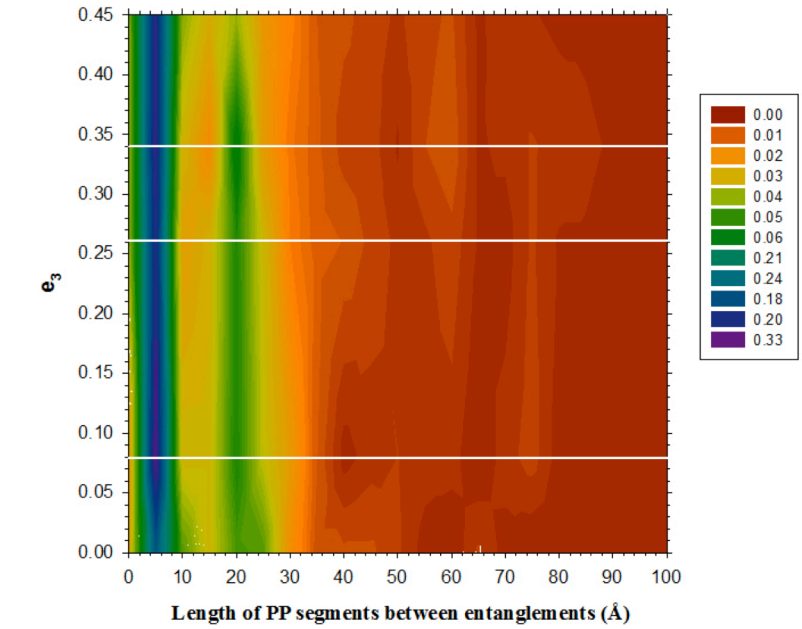

(a)

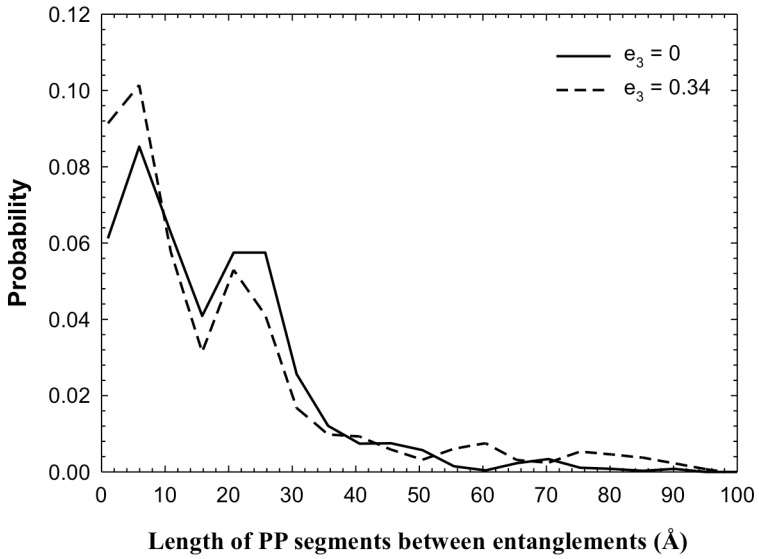

(b)

Figure 8. (a) Length distribution of PP segments between entanglements (Å) as a function of applied strain; horizontal white lines correspond to strains reported in Table 2. (b) Sections of the length distributions in part (a), taken at e_3=0 and e_3=0.34. In both (a) and (b), data has been smoothed using a running average over 5 Å to facilitate comparison.

To illuminate the relationship between the lengthening of PP segments and strain hardening at intermediate extensional strains, we compare in Figure 9 the stress-strain curve of a single configuration with snapshots of PPs in the amorphous domain at selected values of strain. In each snapshot, bridge, loop, and tail segments of PPs were identified. In addition, bridging entanglements such as tail-tail and loop-tail were also identified at each strain. As shown in the snapshots, the lengths of PP segments increase with increasing strain under uniaxial extension. Meanwhile, some bridging entanglements are released during deformation, while others persist. Therefore, we hypothesize that the persistence of bridging entanglements is responsible for the stress-strain response observed at intermediate strain.

In Figure 10, we track the PP of a bridge and show snapshots of it as a function of strain. As shown in the figure, the PP of this bridge segment grows longer with increasing strain. As shown in Figure 9, some bridging entanglements are released during uniaxial extension. However, some of them persist throughout the deformation, and new ones may even be formed. In Figure 11, we show one of these persistent bridging entanglements. As expected, bridging entanglements are stretched during deformation and these persistent bridging entanglements behave similarly to bridge segments ("tie molecules") during deformation. Thus, this kind of persistent bridging entanglements may play an important role in the mechanical response observed here.

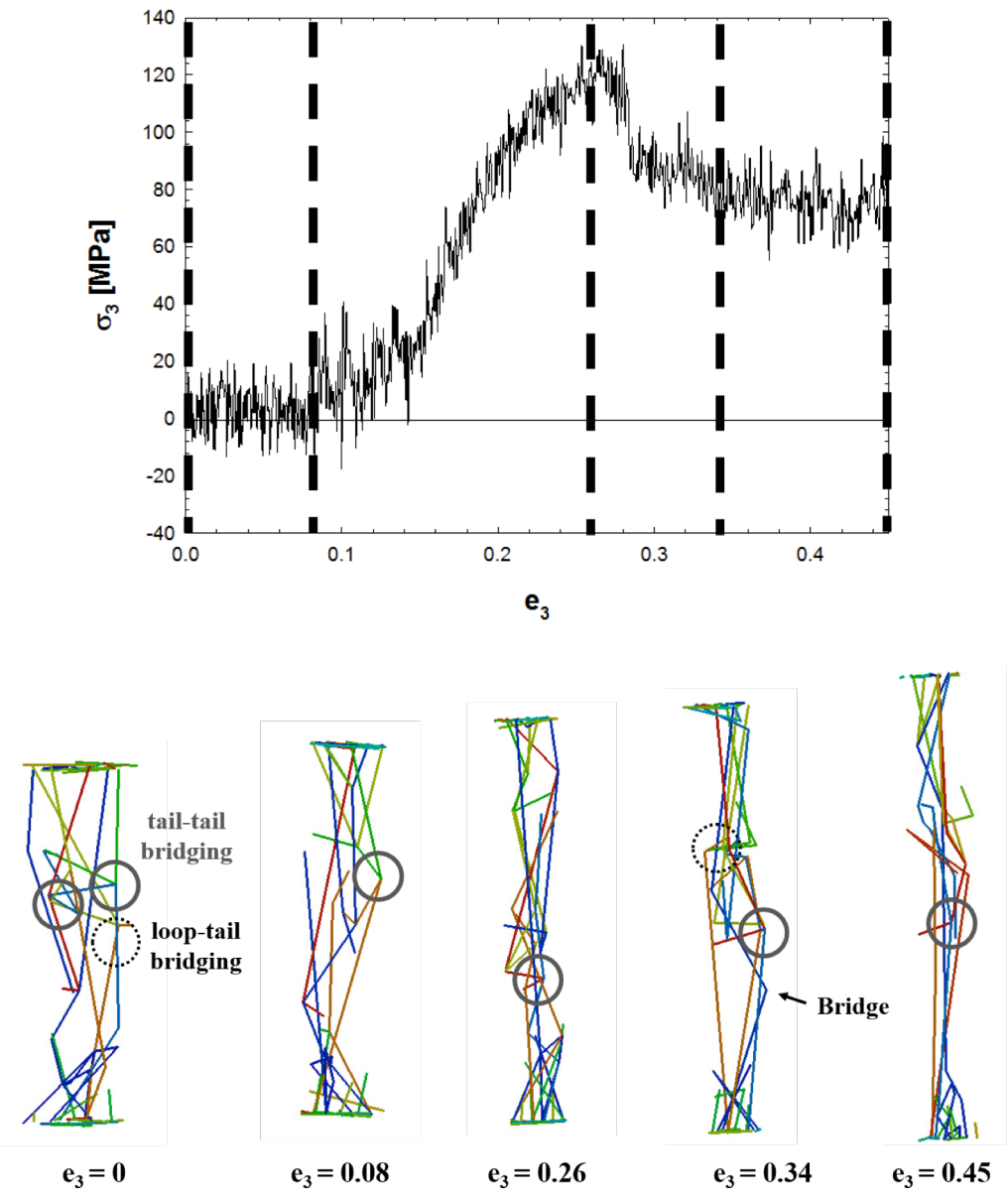

Figure 9. (a) Stress-strain curve for one configuration undergoing fast extensional deformation (unaveraged). (b) Snapshots of the primitive paths in the amorphous domain at strains of e_3=0, 0.8, 0.26, 0.34 and 0.45, for fast deformation in extension (different viewing angles used at each strain to highlight engtanglements). Each snapshot corresponds to one of the vertical dotted lines in stress-strain curve of (a), to show the specific strains where PPs are calculated. Each circle highlights one bridging entanglement and each PP is colored differently to distinguish it from others.

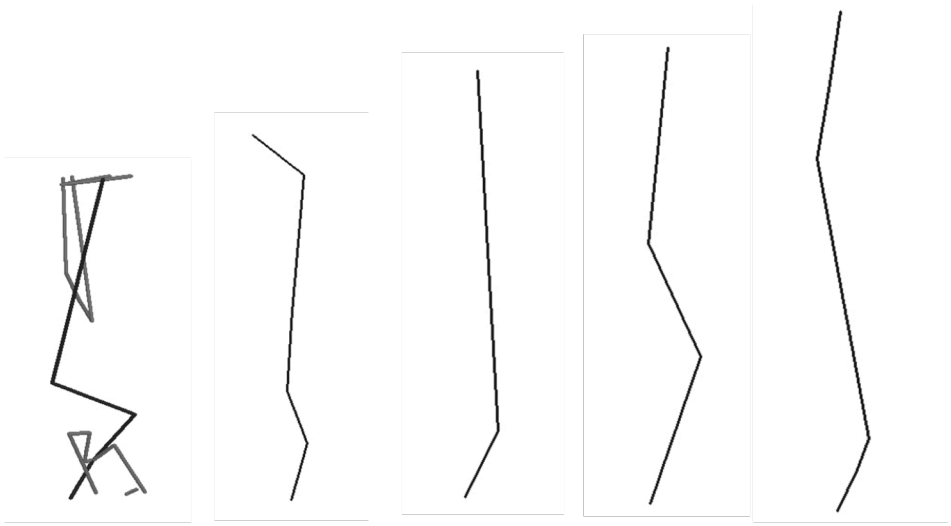

Fig 10. Primitive path of a bridge as function of strain (same trajectory as Fig 9). At zero strain, the heavy black line indicates the original primitive path of the bridge that is subsequently shown at higher strains.

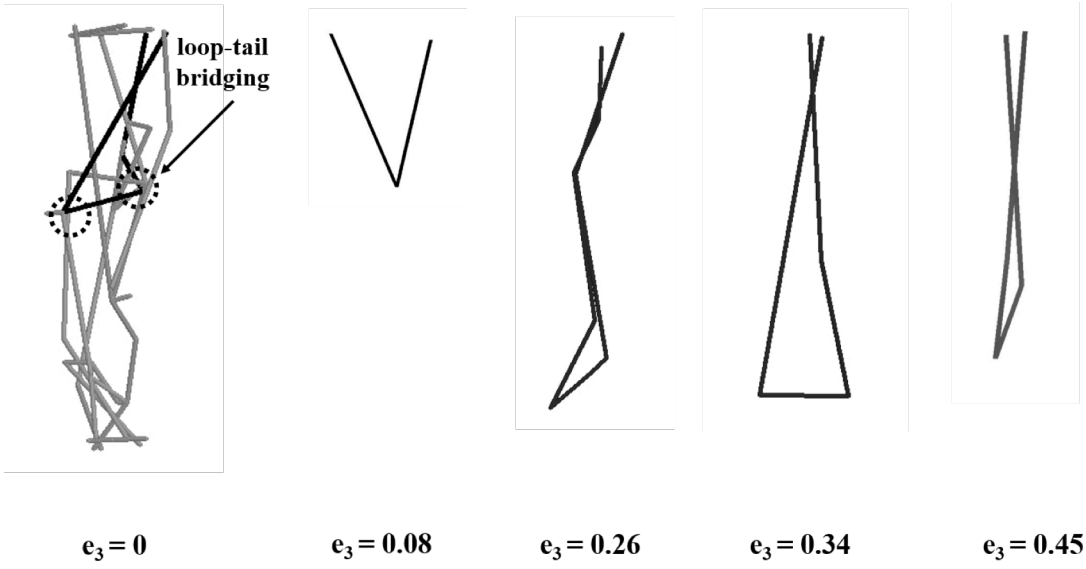

Figure 11. Primitive path of a loop-tail bridging entanglement as a function of strain (same trajectory as Fig 9). At zero strain, the heavy black line indicates the original primitive path of the loop that is subsequently shown at higher strains.

In Figure 12, we compare the stress-strain curve of a single configuration with snapshots of PPs in the amorphous domain at selected values of strain during compression. As shown in the snapshots, during compression most of the bridging entanglements are releasing rather than tightening.

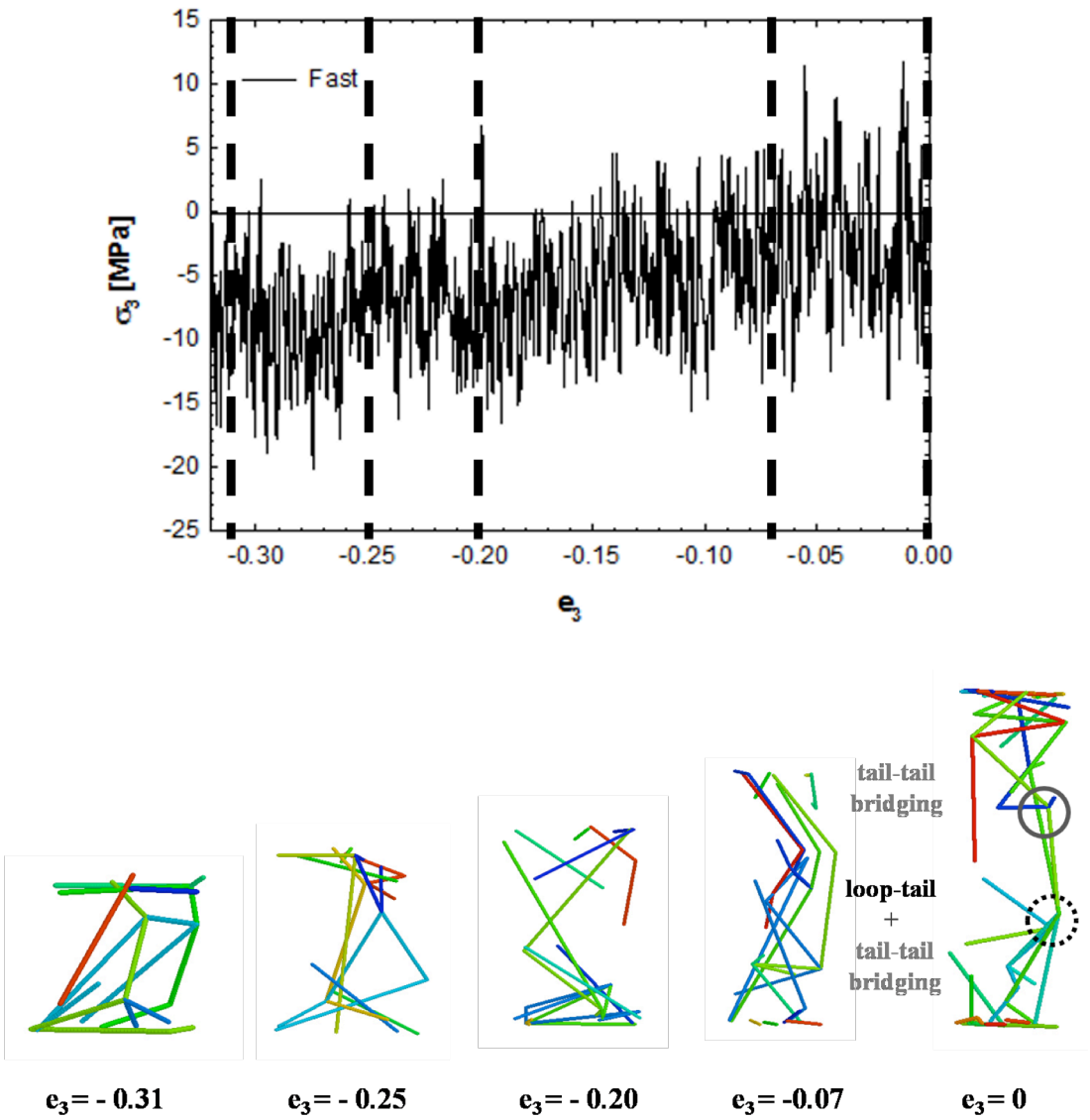

Figure 12. Stress-strain curve of a single configuration under uniaxial compression and primitive paths (PPs) in the amorphous domain at specified strains (different viewing angles).

Crystallinity of the lamellar stack during both fast and slow deformations is shown as a function of strain in Figure 13. Before deformation, the average crystallinity was 53.7%, as mentioned in the section on Topological Analysis. During both fast and slow extensional deformation, the crystallinity remains relatively unchanged up to $e_3 = 0.2$, at which point the crystallinity begins to decrease. This small drop of crystallinity appears to be due to surface melting (a localized melting at the crystal-amorphous interface). This localized melting is also supported by the order parameter analysis and the non-affine displacement of the Gibbs dividing surface, discussed in the next section. This trend in crystallinity, especially for the slow extension case, is very similar to that reported previously[1]. With the onset of twinning at higher strains, recrystallization occurs.

On the compression side, slow deformation leads to a modest rise in crystallinity, whereas fast deformation exhibits little or no change in crystallinity. The rise in crystallinity is attributed to surface crystallization, the converse of surface melting, in response to densification of the system. This rise in crystallinity is precluded under fast deformation, we believe, due to jamming and suppression of secondary nucleation, by analogy to the rapid compression of liquids that is known to suppress primary nucleation and produce a range of amorphous metastable structures[45].

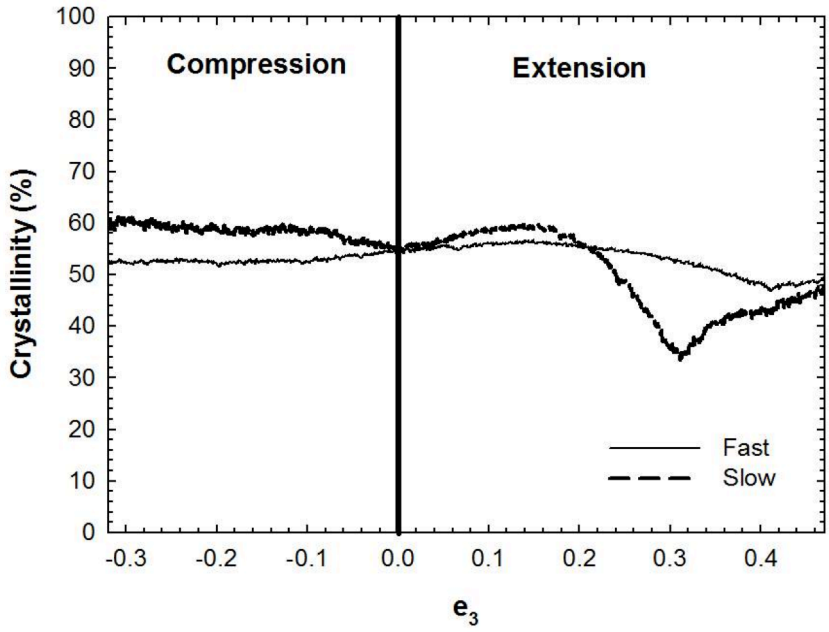

Figure 13. Crystallinity vs. strain for both fast and slow deformations. Strains in both extension and compression are shown.

Figure 14 displays the profiles of local order parameter (P_2) evaluated as a function of both position in the stack direction and strain, for both fast and slow deformations. Results are shown for both extension and compression. From the variation of P_2 with position and strain (or time), it is possible to track the location of the Gibbs dividing surface between the crystal and noncrystalline regions, and thus examine the apportioning of strain into the crystal and noncrystalline domains, respectively. Up to an intermediate strain of $e_3 = 0.20$-0.25, the deformation appears to be affine regardless of deformation rate; each domain experiences the same strain. Beyond this intermediate strain, displacement of the Gibbs dividing surface is hyper-affine, indicative of either surface melting or softening of the noncrystalline domain; however, the surface melting interpretation accords with the observed change of crystallinity vs. strain in Figure 13, and with the onset of yielding. According to Ward[46], the yield process in polymers is a type of softening that may be attributed to a local rise in temperature; the

onset of surface melting coincident with yield is consistent with this interpretation. In contrast to the fast extensional deformation, the slow extensional deformation appears to recrystallize after $e_3 = 0.30$. Under fast and slow compression (Figure 14 (c) and (d), respectively) both crystalline and noncrystalline domains seem to deform affinely. The small amount of recrystallization observed in Figure 13 is only slightly visible in Figure 14 (d) under slow deformation.

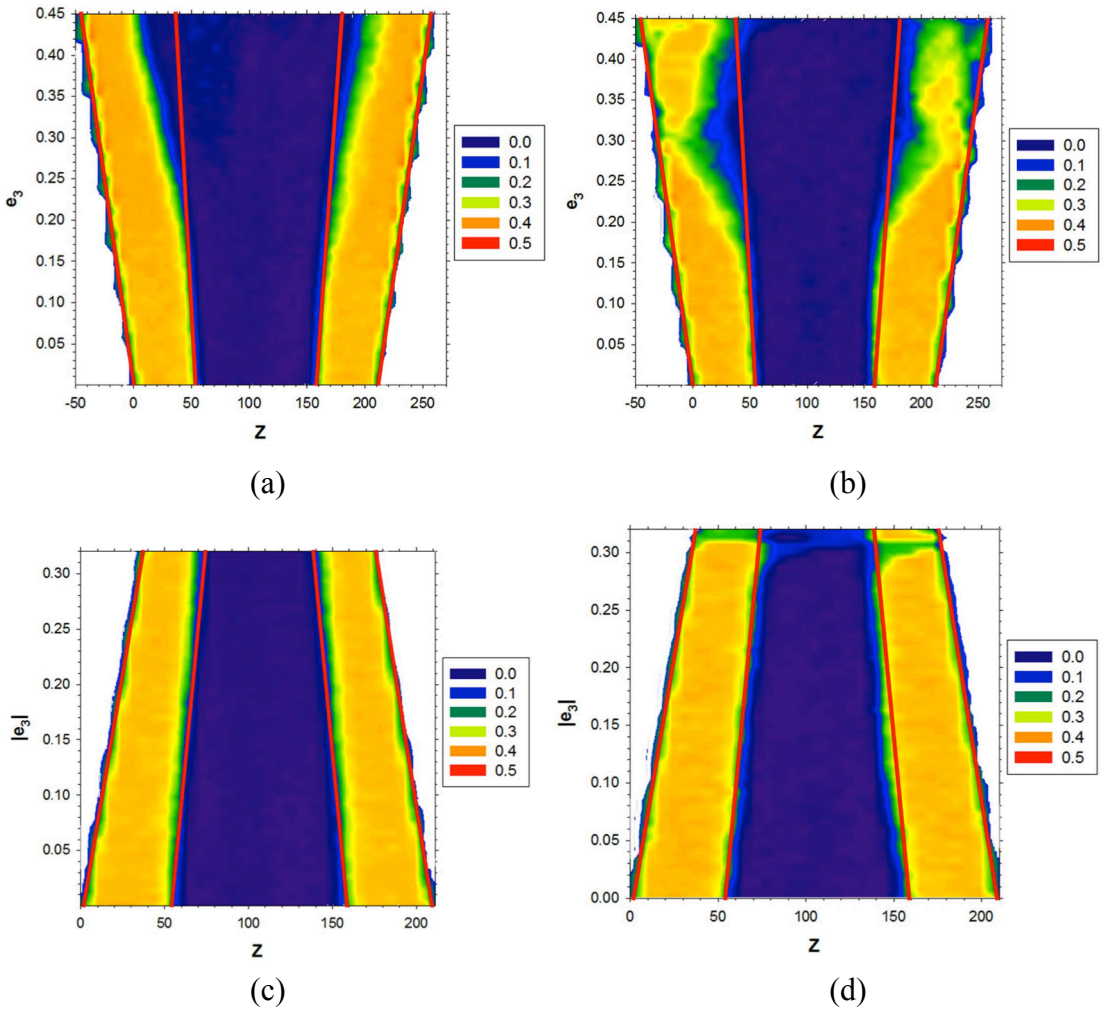

Figure 14. Local order parameter profiles $P_2(z,e_3)$. (a) Fast deformation under tension, (b) Slow deformation under tension, (c) Fast deformation under compression, (d) Slow deformation under compression. The red lines indicate the displacement of the Gibbs dividing surface under the assumption of affine deformation.

Summarizing the behavior under extension and compression up to this point, at small extensional strains ($0 < e_3 < 0.08$) the mechanical response of the lamellar stack is primarily due to fine crystallographic slip in the chain-tilted lamellae rather than elastic deformation in the noncrystalline region, for both of the strain rates considered. As the mechanism of fine crystallographic slip becomes exhausted, deformation is then dominated by stretching of

bridge segments and bridging entanglements for strains of $0.08 < e_3 < 0.18$, as evidenced by the increase in length and alignment of PP segments between entanglements in Figure 8 and the snapshots of PP's in the amorphous domain in Figures 9-12. Between $0.18 < e_3 < 0.26$, entanglement stretching gives way to melting of the crystal domains in the case of slow deformation, beginning at the crystal-amorphous interface. In the case of fast deformation, melting is not significant; instead, stretching of entanglements gives way to cavitation and large plastic deformation. For the slow deformation at high strains ($e_3 > 0.26$), the disappearance of the peak associated with the crystal domain indicates massive melting and reconstruction of the crystal-amorphous interface, previously attributed to crystallographic twinning[1]. By contrast, no such melting and reconstruction is observed under fast deformation. Under compression, fine crystallographic slip plays an important role for response of system over the entire range of compressive strains, regardless of deformation rate.

3. Transverse shear deformation

Transverse shear deformation, or shear deformation parallel to the crystal-amorphous interface, is one of the most important modes of deformation within the spherulitic morphology. Shear deformation is volume-conserving, so it should also be cavitation-free. Due to the inhomogeneous nature of the semicrystalline material, displacement of the z-surface in the x- (or y-) direction (zx or zy shear) is no longer equivalent to displacement of the x- (or y-) surface in the z-direction (xz or yz shear). Nevertheless we continue to employ the more concise Voigt notation with the understanding that zx (Voigt notation: 4) and zy (Voigt notation: 5) were performed in this work.

In Figure 15, stress-strain curves are plotted for the slow strain rate in zx and zy shears. Stress-strain curves for fast shear are qualitatively similar and omitted for brevity. There are

several important points to be noted about these transverse shear simulations. First, although the shear directions are different, the stress-strain responses are similar, indicative of nearly transverse isotropy. Second, stress increases gradually with increasing shear strain in both shear directions. The normal stress (σ_1) increases faster than shear stress (σ_4 or σ_5) in both cases. The stiffness constants (C_{ij}, where j = 4 or 5) can be estimated from the linear response of stress versus strain for both shear directions, and are generally found to be quite small, approaching the limit of resolution of the simulation. Under zx shear, the stiffness constants, C_{15} and C_{55} are found to be 0.083 GPa and 0.008 GPa, respectively. Under zy shear, the stiffness constants, C_{14} and C_{44} are found to be 0.072GPa and 0.006 GPa, respectively. These values of stiffness constants are one to two orders of magnitude smaller than the stiffness in extension or compression of the stack, and as much as 20-fold smaller than the values previously reported from Monte Carlo simulations[13]. As discussed below, the explanation for this difference lies in the thermalization of the crystalline domain, which permits stems to slide along their chain axes within the crystal domain in response to stresses transmitted from the noncrystalline domain, a response not captured by the Monte Carlo simulations with static crystal domains.

The total number of UA in each segment type is presented in Figure 16 as functions of strain for fast deformations under shear in xz. The total number of UA in bridges increases as strain increases, whereas the numbers of UA in loops and tails decrease with increasing strain in Figure 16(a). These changes in length of each segment type may be understood with the help of Figure 16(b). As the crystalline domains are displaced relative to one another, longitudinal sliding of stems within the crystal permit the bridges to lengthen at the expense of loops and tails; a labeled bridge site located at the Gibbs dividing surface prior to deformation may be found within the noncrystalline domain after some finite amount of shear strain. This translational mobility in the crystalline domain is associated with the well-known

α_c-relaxation observed by both experiments and simulations[47-52]. Since the UA model used in this work lacks explicit hydrogens and produces a rotator phase in the crystal domain; it is likely to overestimate the dynamics of pullout of stem segments within the crystal domain, thereby leading to some underestimation of the shear moduli.

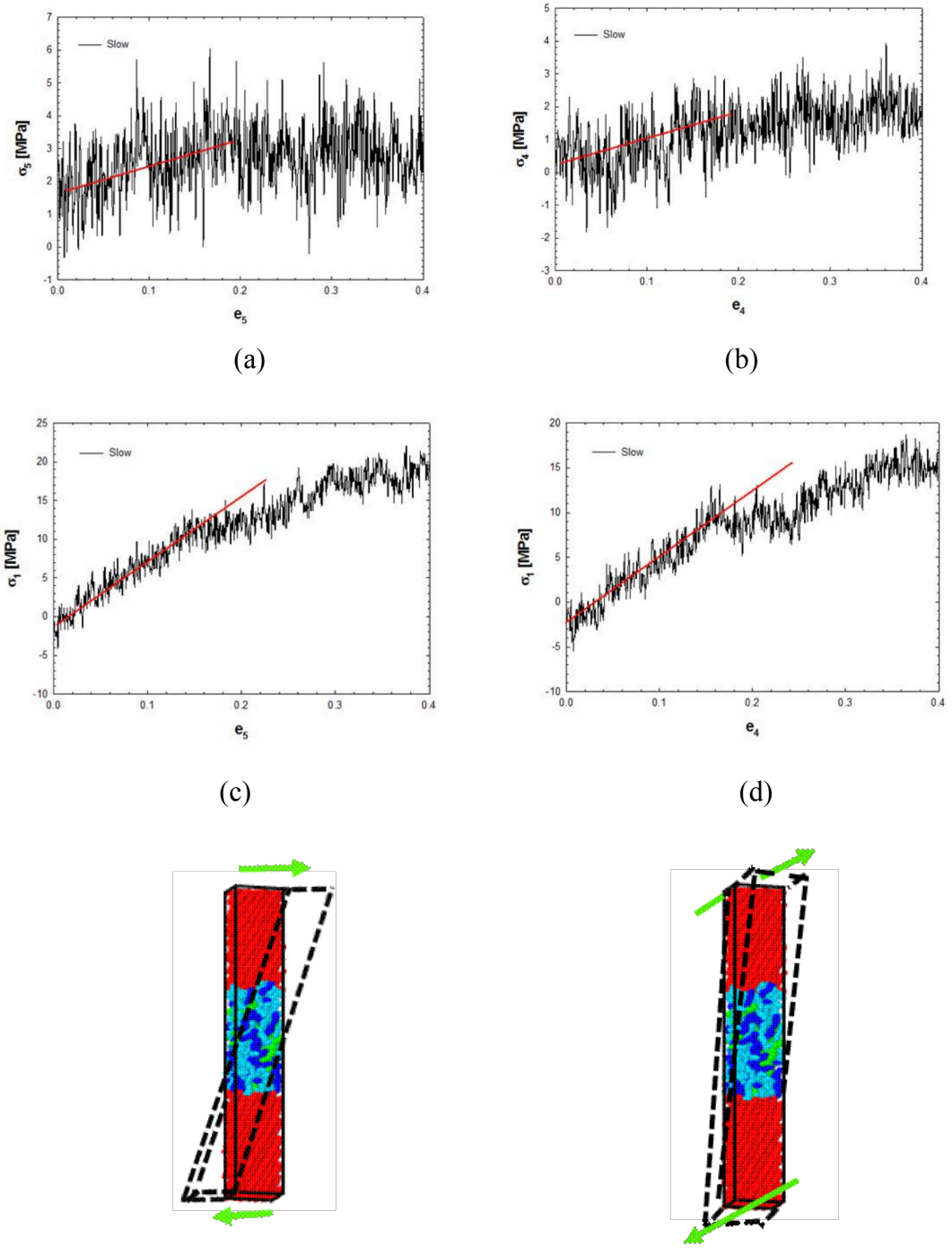

Figure 15. Stress-strain curves under shear in zx, averaged over 10 trajectories; (a) σ_5 vs. e_5, (c) σ_1 vs. e_5. Stress-strain curves under shear in zy; (b) σ_4 vs. e_4, (d) σ_1 vs. e_4.

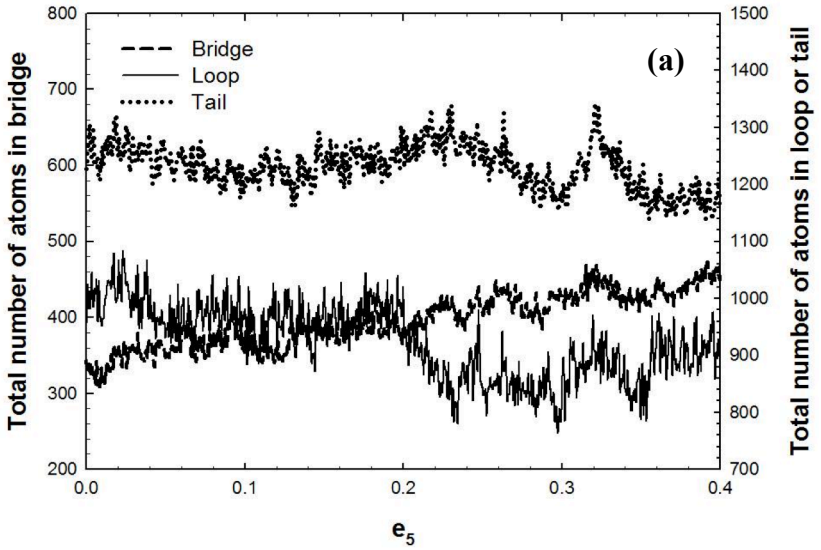

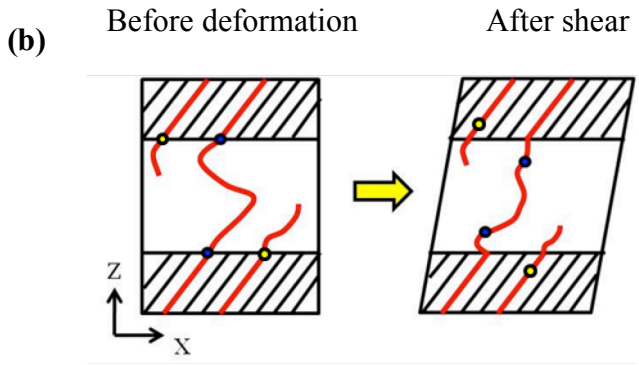

Figure 16. (a) Number of sites in different types of segments vs. strain (e_5) for fast zx shear deformation. (b) Explanation for the lengthening of bridges at the expense of loops and tails during shear; highlighted sites at the interface at e_5=0 are illustrated displaced into the noncrystalline or crystalline domains at some later, finite strain e_5.

Figure 17 shows the evolution of crystallinity for fast and slow deformations in zx and zy shear. For both cases of fast shear deformation, the crystallinity is essentially unchanged. For both cases of slow shear deformation, the crystallinity increases by 4 to 5% with increasing strain because of crystallization at the crystalline-amorphous interface.

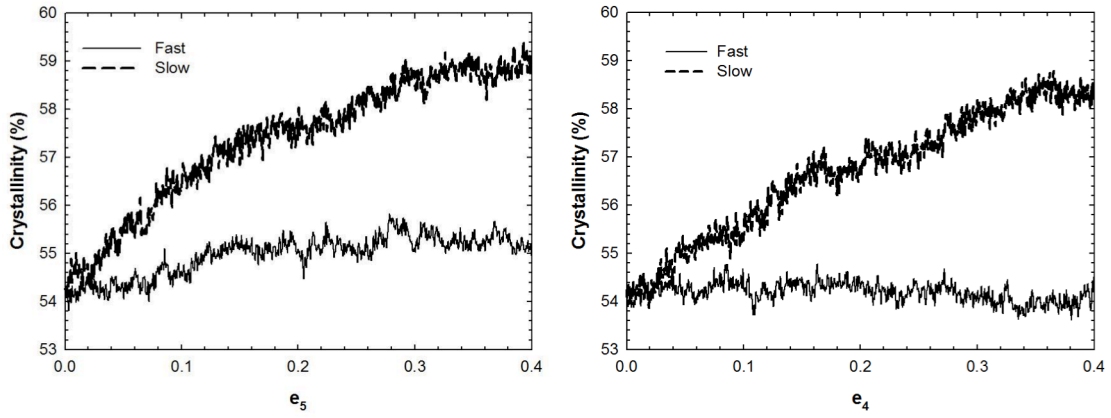

Figure 17. Crystallinity vs. magnitude of strain for fast and slow deformations under shear in (a) zx and (b) zy

In summary, none of the structural changes in the crystalline domain observed during extension or compression, such as crystallographic slip, twinning or martensitic transformation, are observed during shear deformation; instead, response is concentrated in the amorphous domain, facilitated by displacements of chain stems within the crystal, and is essentially isotropic for shears transverse to the lamellar stack direction. Qualitatively, there are similarities in the non-Newtonian response observed here for the topologically constrained interlamellar noncrystalline domain and that of a confined, polymeric melt. One observes an initial, shear rate-dependent, elastic-like component, followed by a visco-plastic response at large strain, with no significant strain hardening apparent over the range of shear strains and shear rates employed here. However, a more complete analysis of this behavior will require additional study.

Conclusion

In this work, we have performed molecular dynamics simulations of a semicrystalline

polyethylene undergoing various modes of deformation, including uniaxial extension, uniaxial compression, and two modes of transverse shear. For continuity with a previous study[1], the same semicrystalline model that thermalized both crystalline and noncrystalline domains was used in this work. Many mechanical and structural properties of the semicrystalline lamellar stack, such as stress-strain response, yield stress, local order parameter (P_2), and so on, have been examined. We find that the underlying mechanisms for the stress-strain response of this semicrystalline polyethylene model are several, the relative importance of which depends on deformation mode, rate of strain, and magnitude of strain.

At low strains, fine crystallographic slip plays an important role in the response of semicrystalline polyethylene under uniaxial extension and compression. At intermediate extensional strains, bridges and bridging entanglements in the noncrystalline domain are responsible for the dramatic increase of stress with strain. However, there is no dramatic increase of stress at the same magnitudes of strain in uniaxial compression, due to the ease of crystallographic slip and releasing of bridging entanglements. Yield occurs at different levels of intermediate strain, depending on strain rate, due to the different mechanisms responsible for yield in each case. As known from the previous study[1], yield occurs with cavitation during fast deformation, whereas yield occurs with surface melting during slow deformation. Yield stresses and yield strains obtained from the constant lateral stress ensemble employed here are higher than those previously reported using a constant volume ensemble[1]. At high strain, crystallographic twinning and recrystallization is observed for slow deformation, in accord with the previous study, whereas melting is observed to accompany cavitation during fast deformation.

As expected, interlamellar slip in the noncrystalline domain is observed during both zx and zy shear. During shear, chain sliding in the crystalline domain is observed to accompany

shear in the noncrystalline domain. This chain sliding is attributed to the α_c-relaxation, which is sufficiently fast to permit lengthening of the bridges and bridging entanglements during both slow and fast shear, rather than their being pulled taut. Under shear deformation, bridging entanglements might be released. Therefore, we may not see a dramatic increase of stress. Stiffness constants are calculated for both zx and zy shear and found to be considerably smaller than reported previously[13], due to the coupling of shear deformation in the noncrystalline domain to chain sliding in the crystalline domain. In shear, this semicrystalline polyethylene model shows shear rate-dependent behavior typical of a polymer melt, even though the chain segments are attached to the crystal domains.

Acknowledgements

Financial support for this work from ExxonMobil Research and Engineering Co. is gratefully acknowledged. We are also grateful to Dr. Vaibhaw Kumar for helpful discussions.

Reference

(1) Lee, S.; Rutledge, G. C. *Macromolecules* **2011**, 44, 3096-3108.

(2) Strobl, G. R. *The Physics of Polymers: Concepts for Understanding Their Structures and Behavior*; Springer: New York,1997.

(3) Flory, P. J.; Yoon, D. Y.; Dill, K. A. *Macromolecules* **1984**, 17, 862-868.

(4) Mandelkern, L. *Macromolecular Chemistry* **1992**, 3, 347-375.

(5) Baker, A. M. E.; Windle, A. H. *Polymer* **2001**, 42, 667-680.

(6) Keller, A. *Philos Mag* **1957**, 2, 1171-1175.

(7) Till, P. H. *J Polym Sci* **1957**, 24, 301-306.

(8) Brooks, N. W. J. and Mukhtar, M. *Polymer* **2000**, 41, 1475-1480.

(9) Lin, L.; Argon, A. S. *J Mater Sci* **1994**, 29, 294-323.

(10) Galeski, A. *Prog. Polym. Sci.* **2003**, 28, 1643-1699

(11) Flory, P. J. *J Am Chem Soc* **1962**, 84, 2857-2867.

(12) Balijepalli, S.; Rutledge, G. C. *J Chem Phys* **1998**, 109, 6523-6526.

(12) Hütter, M.; in 't Veld, P. J.; Rutledge, G. C. *Polymer* **2006**, 47, 5494-5504.

(13) In't Veld, P. J.; Hütter, M.; Rutledge, G. C. *Macromolecules* **2006**, 39, 439-447.

(14) Oleinik, E. F. *Polym Sci Ser* **2003**, C45, 17-117.

(15) Bartczak, Z.; Galeski, A. *Macromol Symp.* **2010**, 294-I, 67-90.

(16) Lacks, D. J.; Rutledge G. C *J Phys Chem* **1994**, 98, 1222-1231.

(17) Kotelyanskii, M.,; Theodorou, D. N. *Simulation Methods for Polymers*; CRC press: New York, 2004

(18) Lee, B.J. et al, *Polymer* **1993**, 34(17), 3555-3575.

(19) Van Dommelen et al, *Polymer* **2003**, 41(19), 6089-6101.

(20) Ghazavizadeh, A. et al, *J. Polym. Sci. Polym. Phys. Ed* **2013**, 51, 1228-1243.

(21) Gautam, S.; Balijepalli, S.; Rutledge, G. C. *Macromolecules* **2000**, 33, 9136-9145.

(22) Rutledge, G.C. *J Macromol Sci Phys* **2002**, B41, 909-922.

(23) Balijepalli, S.; Rutledge, G. C. *Comput Theor Polym* **2000**, S10, 103-113.

(24) In 't Veld, P. J.; Rutledge, G. C. *Macromolecules* **2003**, 36, 7358-7365.

(25) Paul, W.; Yoon, D. Y.; Smith, G. D. *J Chem Phys* **1995**, 103, 1702-1709.

(26) Bolton, K.; Bosio, S. B. M.; Hase, W. L.; Schneider, W. F.; Hass, K. C. *J Phys Chem* **1999**, B103, 3885-3895.

(27) Yi, P.; Locker, C.R.; Rutledge, G.C., *Macromolecules* **2013**, 46, 4723-4733.

(28) Gaur, U.; Wunderlich, B., *Macromolecules* **1980**, 13(2), 445-446.

(29) Yi, P. and Rutledge, G. C. *J Chem Phys* **2011**, 135, 024903-11.

(30) Bassett, D.C.; Hodge, A.M. *Proc. R. Soc. London,* A **1981**, 377, 25 (1981)

(31) Plimpton, S. *J Comput Phy* **1995**, 117, 1-19.

(32) Evans, D. J.; Morriss, G. P. *Statistical Mechanics of Nonequilibrium Liq*uids; Academic Press: New York, 1990

(33) Verlet, L. *Phys Rev* **1967**, 159, 98-103.

(34) Irving, J. H.; Kirkwood, J. G. *J Chem Phys* **1950**, 18, 817-829.

(35) Pope, D. P.; Keller, A. *J. Polym. Sci. Polym. Phys. Ed.* **1975**, 13, 533-566.

(36) Keller, A.; Pope, D. P. *J Mater Sci* **1971**, 6, 453-478.

(37) Brown E.N. et al, *Exper. Mech*. **2007**, 47, 381-393.

(38) Furmanski, J.; Cady, C.M; Brown, E.N, *Polymer* **2013**, 54, 381-390.

(39) Kröger, M*., Comput. Phys. Commun.* **2005**, 168 209-232.

(40) Nilsson, F.; Lan, X.; Gkourmpis, T.; Hedenqvist, M.S.; Gedde, U.W. *Polymer* **2012**, 53, 3594-3601.

(41) Boyd, R. *Polymer* **1985**, 26, 323-347.

(42) Popli, T.; Glotin, M.; Mandelkern, L., Journal *of Polymer Science: Polym. Phys. Ed.*, **1984** 22, 407-448.

(43) Men, Y.; Rieger, J.; and Strobl, G. *Phys. Rev. Lett.* **2003**, 91, 095502-1-4.

(44) Baig, C.; Mavrantzas, V.G.; Kröger, M., *Macromolecules* **2010**, 43, 6886-6902.

(45) Torquato, S.; Stillinger, F. H. *Rev. Modern Phys* **2010**, 82, 2633-2672.

(46) Ward, I. M. *Mechanical Properties of Solid Polymers*; John wiley & sons: New York, 1985.

(47) McCrum, N.G.; Read, B.E.; Williams, G. *Anelastic and Dielectric Effects in Polymeric Solids*; John Wiley and Sons: New York, 1967

(48) Boyd, R. *Polymer* **1985**, 26, 1123-1133.

(49) Hu, W.G.; Schmidt-Rohr, K *Acta Polym.* **1999**, 50, 271-285.

(50) Hu, W.G.; Boeffel, C.; and Schmidt-Rohr, K. *Macromolecules* **1999**, 32, 1611-1619.

(51) Mowry, S.W.; Rutledge, G.C. *Macromolecules* **2002**, 35, 4539-4549.

(52) Zubova, E.A.; Balabaev, N.K.; Manevitch, L.I. *J. Exper. Theor. Phys.* **2002**, 94, 759-769.

Table of Contents Graphic:

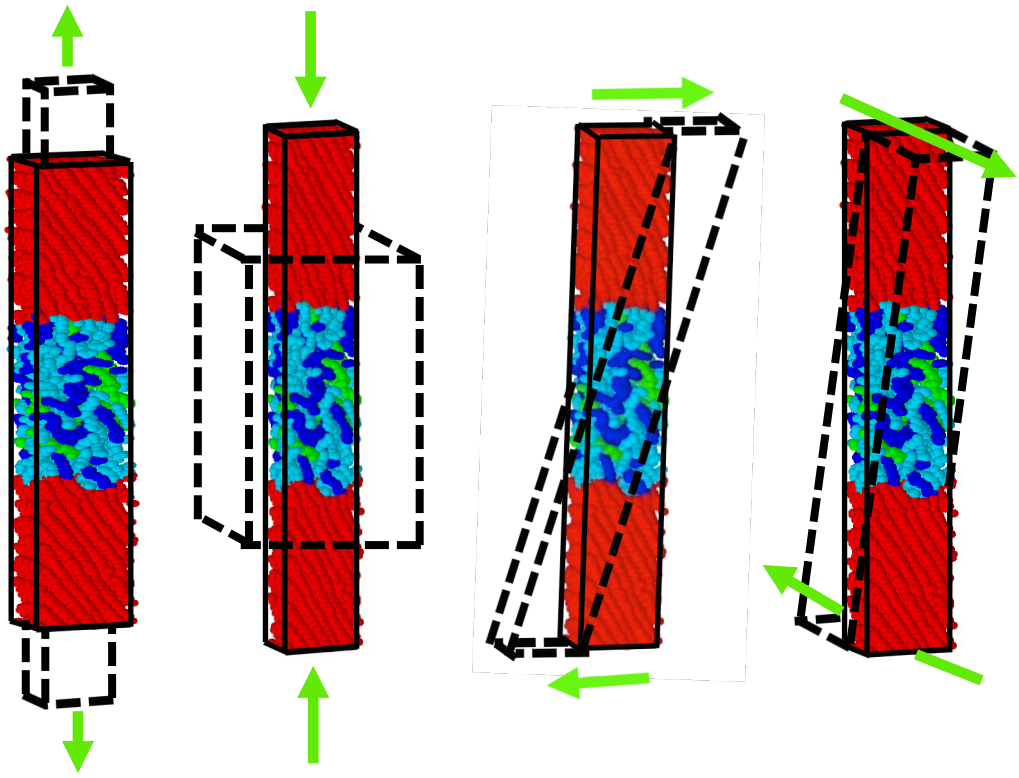

Plastic Deformation of Semicrystalline Polyethylene under Extension, Compression, and Shear using Molecular Dynamics Simulation

Jun Mo Kim, Rebecca Locker and Gregory C. Rutledge